photonics

MDPI

Article

Theoretical Study of Multicascade Raman Microlasers Based on TeO_2–WO_3–Bi_2O_3 Glass

Elena A. Anashkina, Maria P. Marisova and Alexey V. Andrianov *

A. V. Gaponov-Grekhov Institute of Applied Physics of the Russian Academy of Sciences, 46 Ulyanov Street, 603950 Nizhny Novgorod, Russia; elena.anashkina@ipfran.ru (E.A.A.)
* Correspondence: andrian@ipfran.ru

Abstract: The development and investigation of miniature narrow-line coherent light sources based on microresonators with low-power-consumption whispering gallery modes (WGMs) is an actual trend in modern photonics. Raman WGM microlasers can operate at wavelengths inaccessible to traditional laser media and provide a huge pump frequency tuning range. Here, we propose and theoretically study multicascade Raman microlasers based on soft tellurite TeO_2–WO_3–Bi_2O_3 glass WGM microresonators (microspheres) which can operate in the near-IR and mid-IR with the pump in the telecommunication range. Thanks to a large Raman gain (120 times exceeding the maximum Raman gain of silica glass) and a huge Raman frequency shift of 27.5 THz for this glass, the Raman waves at 1.83 μm, 2.21 μm, 2.77 μm, and 3.7 μm in the first, second, third, and fourth cascades, respectively, are theoretically demonstrated with a pump at 1.57 μm. We analyze in detail the influence of different factors on the characteristics of the generated Raman waves, such as microsphere diameters, Q-factors, pump powers, and detuning of the pump frequency from exact resonance. We also solve a thermo-optical problem to show that the temperature of a soft glass microresonator heated due to partial thermalization of pump power remains below the glass transition temperature. To the best of our knowledge, mid-IR tellurite glass Raman WGM microlasers have not been studied before.

Keywords: Raman lasing; tellurite glass; microlaser; microresonator; whispering gallery modes

check for updates

Citation: Anashkina, E.A.; Marisova, M.P.; Andrianov, A.V. Theoretical Study of Multicascade Raman Microlasers Based on TeO_2–WO_3–Bi_2O_3 Glass. *Photonics* **2023**, *10*, 1137. https://doi.org/10.3390/photonics10101137

Received: 14 September 2023
Revised: 4 October 2023
Accepted: 7 October 2023
Published: 11 October 2023

1. Introduction

The development of narrow-linewidth near-IR and mid-IR sources of coherent light based on lasing or nonlinear optical effects is in demand for manifold applications and fundamental research. Raman lasers allow generating narrow-line coherent light in spectral ranges inaccessible to "conventional" lasers operating at radiative transitions of rare-earth ions (Yb^{3+}, Er^{3+}, Tm^{3+}, etc.) [1]. In Raman lasers, thanks to inelastic light scattering, the pump light may, in principle, be converted to the low-frequency range throughout the transparency band of a chosen material (with appropriate pump sources) [2,3]. For rare-earth ion-doped lasers, the pump frequency must belong to a certain absorption band of the used rare-earth ions, while there is no such strict limitation on pump frequency for Raman lasers [1]. For Raman lasers, the frequency shift of the generated Raman wave with respect to the pump frequency (Δf_R) depends on the material properties (and often corresponds to the frequency of the maximum gain). It is well known that cascade Raman lasing can be achieved when the generated coherent Raman wave itself serves as a pump for the generation of a second-order coherent Raman wave; then, the generated second-order Raman wave serves as a pump for the generation of a third-order coherent Raman wave, and so on [3,4]. Thus, the frequency of the second-order Raman wave is down-shifted by $2 \times \Delta f_R$ relative to the pump frequency, the frequency of the third-order Raman wave is down-shifted by $3 \times \Delta f_R$, and the frequency of the Nth-order Raman wave is down-shifted by $N \times \Delta f_R$. Therefore, multicascade Raman lasers can provide frequency

tuning in a wide frequency range, which may be important for many applications and fundamental problems.

Raman lasers are based on different materials, including bulk elements made of crystals and glasses [5,6], glass fibers [3,7], gas-filled fibers [8,9], microresonators made of glass and crystalline materials [10,11], gases in cells [12], and others. An active medium and a resonator are frequently required for creating lasers, including Raman ones [1] (although random distributed feedback (DFB) lasers with a mirrorless open cavity are also known [13]). Mirrors and reflective coatings, as well as Bragg gratings in the case of fiber lasers, can serve as a resonator [3]. When working with cascade Raman lasers, a resonator is usually required for each wavelength (exceptions are DFB lasers [14]). For example, for fiber lasers, several pairs of Bragg gratings corresponding to the number of Raman cascades can be used [15]. However, a microresonator with whispering gallery modes (WGMs) is simultaneously a gain medium and a cavity for a Raman microlaser including multicascade ones [10,11,16]. A dielectric resonator with WGMs can trap photons by total internal reflection ensuring light propagation along its equator [10]. Such microresonators have huge Q-factors and large nonlinearity due to extremely small mode volume, which make it possible to attain nonlinear effects at very low pump powers [10,11,16]. It is known that Raman generation is observed in WGM microresonators in many cascades (for example, the number of cascades was five in silica [16] and chalcogenide As_2S_3 [17] microspheres, and eight in a CaF_2 microdisk [18]). At the same time, it is rather problematic to obtain Raman generation with a large number of cascades in more traditional systems with separated active medium and resonators. Therefore, if the development of a miniature, low-power narrow-line coherent light source with a low-power consumption and a huge pump frequency tuning range is required, a multicascade Raman WGM microlaser seems to be an excellent solution.

When developing a Raman WGM microlaser, special attention should be paid to the choice of material, since Raman amplification properties vary greatly for different media. For instance, for a standard silica glass, the maximum gain is 10^{-13} m/W (for a pump wavelength of 1 μm), and the Raman frequency shift corresponding to this value is Δf_R = 13.2 THz [2]. For crystalline materials such as CaF_2 widely used for fabricating WGM microdisks, the maximum Raman gain has the same order but the Raman shift is lower (~10 THz) [18]. In recent years, special soft glasses with huge nonlinearity and a wide transparency range (with mid-IR red border) have been attracting increasing attention. For widespread chalcogenide As_2S_3 and As_2Se_3 glasses, the Raman gains are 4.3×10^{-12} m/W [19] and 5.1×10^{-11} m/W [20], respectively. However, their Raman shifts are relatively low: ~10 THz [19] and ~7 THz [20], respectively. Against this background, special tellurite glasses with a transparency band of ~0.5–5 μm and Raman gains of two orders of magnitude higher than the value for silica glass and the frequency shift corresponding to a maximum of 20–28 THz [21,22] seem to be very promising materials for the implementation of multicascade mid-IR WGM microlasers, even with a pump wavelength belonging to the well-mastered telecommunication range. We recently demonstrated Raman lasing in a tellurite TeO_2-WO_3-La_2O_3 (TWL) microsphere (for the first time for tellurite microresonators) [23]. In this case, the maximum wavelength in the second cascade was 2.01 μm with a pump at 1.57 μm [23]. It should be noted that we previously achieved the same wavelength with the same pump source in a chalcogenide As_2S_3 microsphere but in the fourth cascade [24]. In both cases, we used a silica fiber taper to extract the generated Raman waves. This taper has huge losses at wavelengths >2 μm, so we could not register generation in higher cascades.

Here, we propose and theoretically study multicascade Raman microlasers based on TeO_2–WO_3–Bi_2O_3 (TWB) glass with a maximum Raman gain 120 times exceeding the maximum Raman gain of silica glass [22]. This glass also has a huge Raman frequency shift of Δf_R~27.5 THz [22], which allows broadband frequency conversion using a reasonable number of cascades. It is important to note that since tellurite glasses have a relatively low glass transition temperature (T_g~370 °C for TWB glass [25]), it is necessary to take into

consideration the heating of the microresonator during partial pump thermalization and to control that the maximum temperature should remain below T_g, which is also taken into account in the simulation. We investigate a realistic design of microlasers and demonstrate numerically their mid-IR operation using a standard telecom pump wavelength. To the best of our knowledge, the mid-IR tellurite glass Raman WGM microlasers have not been previously studied.

2. Materials and Methods

We considered the scheme of a TWB glass WGM microlaser shown in Figure 1a. We assumed that a fiber taper made of tellurite glass was used to couple the pump light and extract the generated coherent Raman waves. The pump wavelength was taken to be 1.57 µm (corresponding to a frequency of 191 THz), as in our previous experimental work [23].

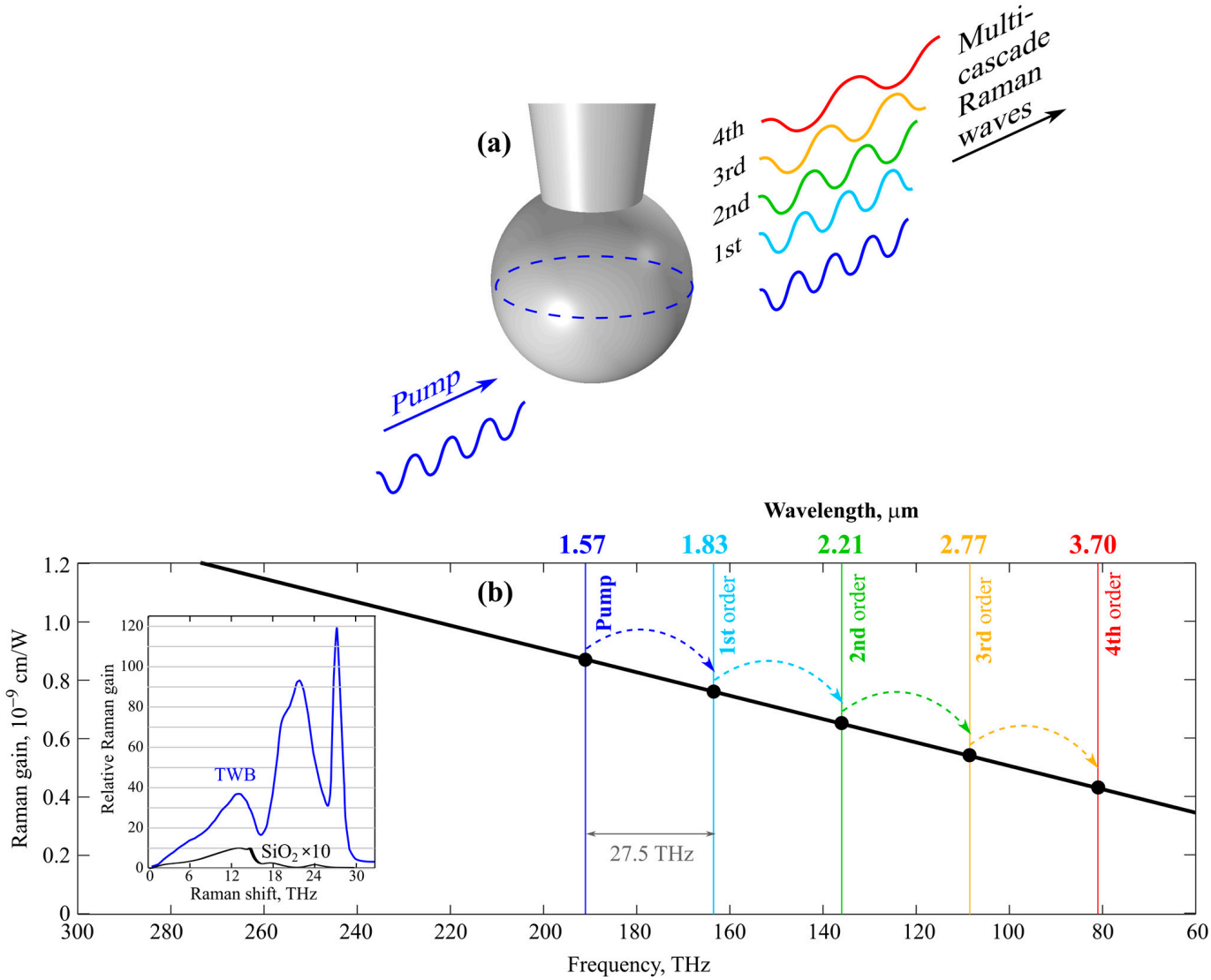

Figure 1. (**a**) Schematic presentation of multicascade Raman lasing in a TWB microsphere using tellurite fiber taper for coupling pump light and for extracting generated waves. (**b**) Maximum Raman gain as a function of pump frequency (black line with circles) and schematic diagram of stimulated multicascade Raman scattering processes in spectral domain. The inset shows Raman gain spectra of TWB glass (blue) compared to silica glass.

The cascade scheme of Raman processes is presented in Figure 1b. We took into account that the maximum Raman gain is inversely proportional to the pump wavelength [2]. The model Raman gain function of TWB glass in comparison with the Raman gain function of silica glass is plotted in the inset in Figure 1b based on the data presented in [22]. The expected frequencies in the Raman cascades were 191 THz − 27.5 THz = 163.5 THz (in the first cascade), 191 THz − 2 × 27.5 THz = 136 THz (in the second cascade), 191 THz − 3 × 27.5 THz = 108.5 THz (in the third cascade), and 191 THz − 4 × 27.5 THz = 81 THz (in the fourth cascade). So, the expected wavelengths of Raman waves in the first, second, third, and fourth cascades were 1.83 µm, 2.21 µm, 2.77 µm, and 3.70 µm, respectively. The fifth cascade was not expected here because the corresponding frequency 191 THz − 5 × 27.5 THz = 53.5 THz (wavelength of 5.6 µm) was beyond the transparency range of TWB glass.

2.1. Numerical Model for Multicascade Raman Lasing

The theoretical study of multicascade Raman lasing according to the scheme shown in Figure 1a was performed using the coupled mode theory for intracavity electric field amplitudes U_k. We used the well-known model for cascade microlasers [16]:

$$\frac{dU_0}{dt} = \left(i\Delta\omega_0 - \frac{1}{2\tau_0}U_0\right) - g_1\frac{\omega_0}{\omega_1}|U_1|^2U_0 + \sqrt{\kappa_0 P}, \tag{1}$$

$$\frac{dU_k}{dt} = -\frac{1}{2\tau_k}U_k + g_k|U_{k-1}|^2\mathrm{U}_k - g_{k+1}\frac{\omega_k}{\omega_{k+1}}|U_{k+1}|^2U_k, \text{ for} k = 1, \ldots, N-1, \tag{2}$$

$$\frac{dU_N}{dt} = -\frac{1}{2\tau_N}U_N + g_N|U_{N-1}|^2\mathrm{U}_N, \tag{3}$$

where U_0 corresponds to the electric field pump wave at angular frequency ω_0 and U_k corresponds to the Raman wave generated in the k-th cascade at angular frequency ω_k; t is the time; $\Delta\omega_0$ is the angular frequency detuning of the pump frequency from the nearest exact resonance; P_0 is the pump power; τ_s is the total photon lifetime at ω_s (s = 0, 1,... N, $\tau_s = Q_s/\omega_s$, where Q_s is the loaded Q-factor); κ_s is the coupling coefficient (we set $\kappa_s = 1/(2 \times \tau_s)$); and g_k is the intraresonator Raman gain coefficient proportional to the maximum Raman gain for bulk TWB glass g_{TWB} with allowance for wavelength scaling (Figure 1b):

$$g_k = \Gamma g_{TWB}c^2/\left[n_{TWB}^2(V_{k-1} + V_k)\right], \tag{4}$$

where c is the speed of light, n_{TWB} is the linear refractive index of TWB glass, V_k and V_{k-1} are effective mode volumes V_{eff} in the kth and $(k-1)$th cascades, and Γ is the overlap factor between the waves in the kth and $(k-1)$th cascades (we estimated and set Γ = 0.7). The effective mode volume V_{eff} for a microsphere with diameter d (Figure 2a) is calculated as

$$V_{eff} = \pi d\frac{\left(\int S_\varphi d^2r\right)^2}{\int S_\varphi^2 d^2r} \tag{5}$$

where S_φ is the azimuthal projection of the Pointing vector and d is the microsphere diameter. For calculating V_{eff} the spatial distribution of the WGM electromagnetic field as well as the WGM eigenfrequency are needed. The eigenmodes of a dielectric sphere are a well-known problem in electrodynamics; the characteristic equations and expressions for electric and magnetic fields can be found in [26]. We solved the characteristic equations numerically to determine the WGM eigenfrequency for a microsphere of a specific diameter near target wavelength. Next, we used it to calculate the electromagnetic field distribution and then performed the integration procedure to obtain V_{eff} as in Equation (5). We considered only TE fundamental WGMs in all calculations. The obtained effective mode volumes V_{eff} as a function of the light wavelength λ for microspheres of different diameter

(d = 40 µm, d = 60 µm, d = 80 µm, and d = 100 µm) are presented in Figure 2b. As expected, the smaller the microsphere, the smaller the effective mode volume.

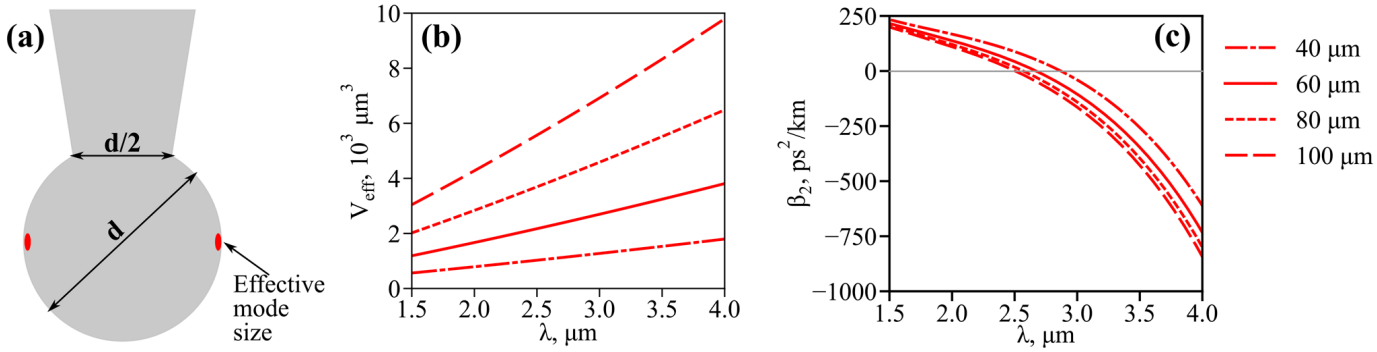

Figure 2. (**a**) Geometry of microsphere. Calculated effective mode volumes (**b**) and second-order dispersion (**c**) vs wavelength λ for different microsphere diameters d.

The output power in a Raman wave is $P_k = \kappa_k |A_k|^2$. We considered continuous wave operation; so, the left-hand sides of Equations (1)–(3) were zero, ($dU_s/dt = 0$). The system of equations became algebraic and was easily solved analytically. We successively considered all regimes of Raman lasing: when only one Raman wave in the first cascade could be generated (in this case, Equations (1) and (3) for $N = 1$ were used); when two Raman waves in the first and second cascades were generated (the system of Equations (1)–(3) was written for three equations at $N = 2$); when three cascades were generated (the system of Equations (1)–(3) was written for four equations at $N = 3$); and when four cascades were generated (the system of Equations (1)–(3) was written for five equations at $N = 4$). As noted above, the Raman lasing in the fifth cascade was not considered, as the corresponding wavelength of 5.6 µm was beyond the transparency band of TWB glass.

We neglected four-wave mixing processes (between pump, Raman Stokes and anti-Stokes photons and other combinations of pump and Raman waves). However, it is known that when phase matching conditions are met, anti-Stokes light components can be generated with reasonable efficiencies in microresonators even with a normal dispersion [27,28]. We checked using the previously implemented model [29] that for our resonators the phase matching conditions are not met. The calculated second-order dispersion coefficients β_2 vs. wavelength are plotted in Figure 2c.

2.2. Numerical Model for Microsphere Heating under Partial Pump Thermalization

The thermo-optical heating was studied using a theoretical model based on finding the temperature distributions in a TWB glass microsphere during pump power thermalization. The corresponding problem of thermodynamics can be expressed via the heat equation [30]:

$$\rho c_p \frac{\partial \Delta T}{\partial t} + div\, \boldsymbol{\phi} = Q \tag{6}$$

$$\boldsymbol{\phi} = -k\nabla(\Delta T), \tag{7}$$

where ΔT is the temperature increase, ρ is the glass density, c_p is the glass heat capacity at constant pressure, $\boldsymbol{\phi}$ is the heat flux density, Q is the heat source, and k is the glass thermal conductivity. We used the following parameters of the tellurite glass: ρ = 5940 kg/m^3, c_p = 370 J/(kg·K), and k = 1.2 W/(m·K).

We developed a numerical model employing the finite element method (FEM) for calculating the spatial distribution of the temperature increase ΔT. As in a real experiment, a microsphere is usually supported by a fiber stem that influences the heat flow, and the calculations were performed for a realistic axially symmetric geometry demonstrated in Figure 2a. It should be noted that Figure 2a shows only a part of the model omitting the

rest of the relatively long (several mm) fiber stem. On all surfaces we chose the boundary condition of free convection in air [30]:

$$\phi_{norm} = -\alpha_{conv}\Delta T, \tag{8}$$

where ϕ_{norm} is the outward-pointing component of the heat flow density vector and α_{conv} is the convection coefficient. We used empirical relations for α_{conv} [30].

We assumed that heating occurs only in a small near-surface region of a microsphere with elliptical cross-section (marked red in Figure 2a); this is done to mimic partial pump power absorption in a highly localized WGM. The total heating power P_{heat} is evenly distributed over this region and its total volume should coincide with the effective mode volume V_{eff}.

3. Results

3.1. Numerical Simulations of Microsphere Heating under Partial Pump Thermalization

First of all, we solved the thermo-optical problem to understand what powers can be used. It is important for us that the temperature of heated microsphere should be notably lower than T_g at the pump power required for generating the fourth Raman cascade. An example of the calculated temperature field (temperature increase) in a microsphere with a diameter of 60 μm at the thermalized power P_{heat} = 4 mW is shown in Figure 3a. It can be seen that the largest temperature increase ΔT~200 K is observed near the equator, but at the same time, this temperature increase in the volume of the microsphere is approximately 10% lower; so, heating occurs fairly evenly. It should be noted that a significant increase in the tellurite microsphere temperature leads to thermal expansion with the coefficient $\alpha = 14 \times 10^{-6}$ K^{-1} and refractive index changes $\Delta n = (dn/dT) \times \Delta T$, where $dn/dT = -8 \times 10^{-6}$ K^{-1}. For a 60 μm microsphere heated to ΔT~200 K, its diameter increase is only Δd~0.17 μm and $\Delta n = -0.0016$. We assumed that the spherical form is preserved with a sufficient accuracy. These changes are too small to alter the general form of Equations (1)–(5). However, it is well known that under the influence of these two factors, a thermo-optical shift of microsphere eigenfrequencies occurs [31]. So, the detuning value $\Delta\omega_0$ in Equation (1) corresponds to a "hot" resonator (in the study presented in Section 3.2 we examine in detail the lasing characteristics as a function of this "hot" detuning).

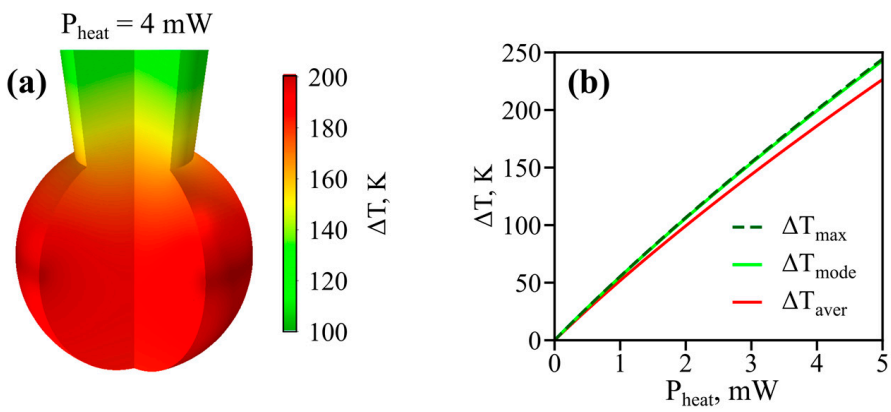

Figure 3. (**a**) Example of temperature increase distribution in a 60 μm microsphere for thermalized power P_{heat} = 4 mW. (**b**) Maximum temperature increase (dashed curve), temperature increase averaged over the effective mode volume (solid green curve), and temperature increase averaged over the microsphere without the stem (red curve).

The maximum temperature increase ΔT_{max}, the temperature increase averaged over the mode volume ΔT_{mode}, and the temperature increase averaged over the microsphere volume ΔT_{aver} as a function of thermalized power P_{heat} are plotted in Figure 3b. The negligible

difference between ΔT_{max} and ΔT_{mode} can be explained by the small effective mode volume that causes a fairly even temperature increase in the pump thermalization region.

Next, we solved the thermo-optical problem for microspheres of different diameters. The curves for the maximum temperature increase as a function of thermalized power for microsphere diameters of 40 µm, 60 µm, 80 µm, and 100 µm are plotted in Figure 4.

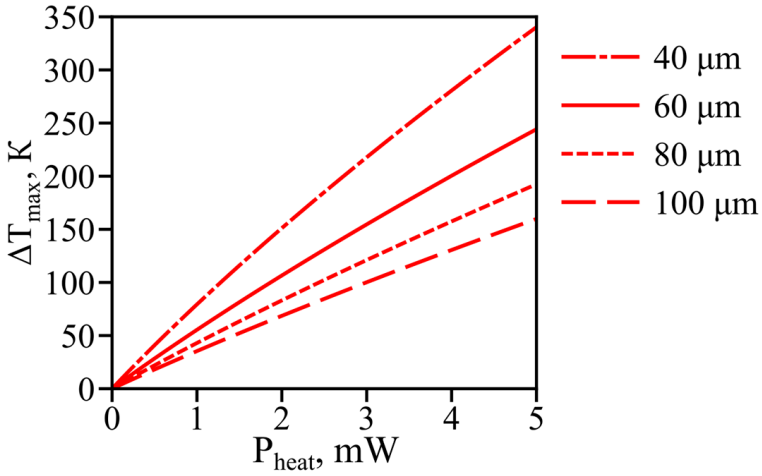

Figure 4. Maximum temperature increase as a function of thermalized pump power P_{heat} for TWB microspheres of different diameters.

The smaller the microsphere, the higher the maximum temperature. The qualitative explanation of this effect is rather straightforward. The total surface area of the microsphere is proportional to d^2. Equation (7) shows that the convective heat flux density $\boldsymbol{\phi}$ on the surface of the microsphere is roughly proportional to the temperature increase ΔT and the convective coefficient α_{conv}. For our conditions, α_{conv} can be approximated as $\alpha_{\text{conv}} \approx 2k_{air}/d$ [30], where k_{air} is the thermal conductivity of air, i.e., α_{conv} is inversely proportional to d. Therefore, the total convective heat flow, which is mostly responsible for the cooling process and can be found by integrating the convective heat flux density over the microsphere surface, is roughly proportional to d. A decrease in d lowers the total heat flow at a given temperature increase; thus, the equilibrium temperature must be higher for compensating the same thermalized power P_{heat}. Despite it being a very rough estimate, it provides a simple qualitative explanation.

3.2. Numerical Simulations of Multicascade Raman Lasing

Multicascade Raman generation was numerically simulated using microspheres of different diameters and with different Q-factors. It should be noted that the highest loaded Q-factor for tellurite microresonators experimentally achieved so far was $Q = 3.7 \times 10^7$ [32]. Raman lasing up to the second cascade inclusive was obtained in a TWL microsphere with loaded Q-factor $Q = 2.4 \times 10^7$ [23]. The threshold pump power P_{thr} for Raman lasing in the first cascade was found from Equations (1) and (2):

$$P_{thr} = \frac{1}{2\kappa_0\tau_0 g_1}\left[\frac{1}{4\tau_0^2} + \Delta\omega_0^2\right]. \tag{9}$$

To obtain (9), we assumed $\tau_0 = \tau_1$ and $\kappa_0 = \kappa_1$. It is seen that for the exact resonance $\Delta\omega_0 = 0$, the threshold pump power is inversely proportional to Q^2; so, the Q-factor is a very important characteristic.

The calculated threshold pump powers as a function of two variables, pump power and pump frequency detuning, for microspheres of different diameters are plotted in Figure 5. The upper row corresponds to the highest considered intrinsic Q-factor $Q = 2.4 \times 10^7$, the middle row corresponds to intermediate value $Q = 1.2 \times 10^7$, and

the bottom row corresponds to the lowest considered Q-factor $Q = 0.5 \times 10^7$. The left column demonstrates the results for the threshold pump powers required to achieve the first-order Raman wave, while the second, third, and fourth columns demonstrate the pump powers required to achieve Raman lasing in the second, third, and fourth cascades, respectively. As expected, the higher the Q-factor, the lower the threshold. The larger the microsphere, the higher the threshold. It should be noted that in the experiment the Q-factors of the manufactured samples of tellurite microsphere were practically independent of their diameters (for d ranging from 30 to 100 μm) [23]. So, on the one hand, it seems that small microspheres are most suitable for multicascade Raman lasing. On the other hand, as demonstrated in Figure 4, the temperature increase for them is maximal. Therefore, we can say that in the experiment it may be better to work with microspheres with intermediate diameters, for example, 60 μm, for which the pump power thresholds are quite low and, at the same time, the temperature remains below T_g.

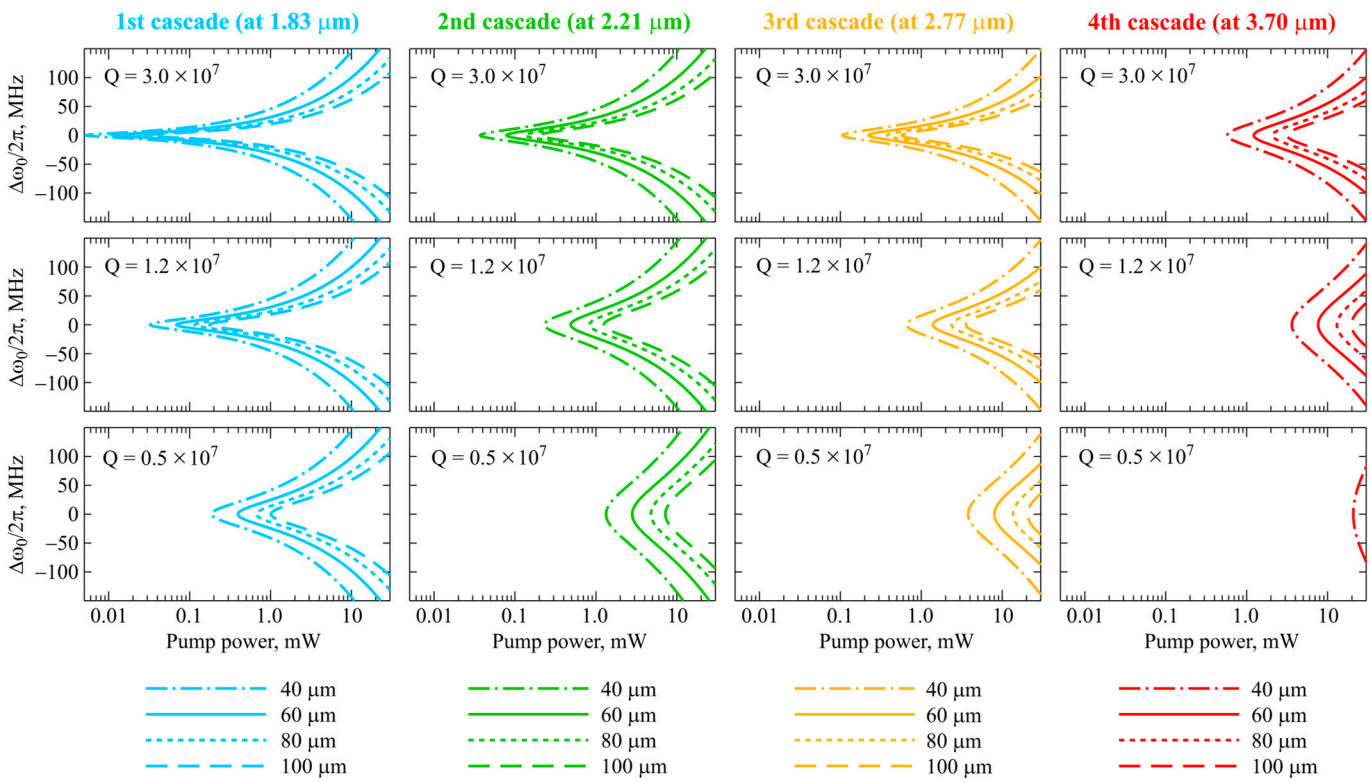

Figure 5. Diagrams demonstrating threshold powers for Raman wave generated in the 1st, 2nd, 3rd, and 4th cascades (each column corresponds to a certain cascade at 1.83 μm, 2.21 μm, 2.77 μm, and 3.70 μm, respectively) for different microsphere diameters (each line style corresponds to a certain diameter) and for different Q-factors (each row corresponds to a certain Q-factor).

Next, we analyzed Raman lasing in more detail specifically in 60 μm microspheres. We chose an intermediate value of the intrinsic Q-factor ($Q = 1.2 \times 10^7$). Figure 6a–d show the Raman wave power in the first, second, third, and fourth cascades, respectively, as a function of two variables: the pump power and the pump frequency detuning from the exact resonance. The red lines in the green planes demonstrate the thresholds (only for the first cascade in Figure 6a, for the first and second cascades in Figure 6b, for the first, second, and third cascades in Figure 6c, and for all four cascades in Figure 6d). It is seen that a sub-mW level of output Raman waves in all cascades can be achieved for a reasonable pump power level of 10 mW.

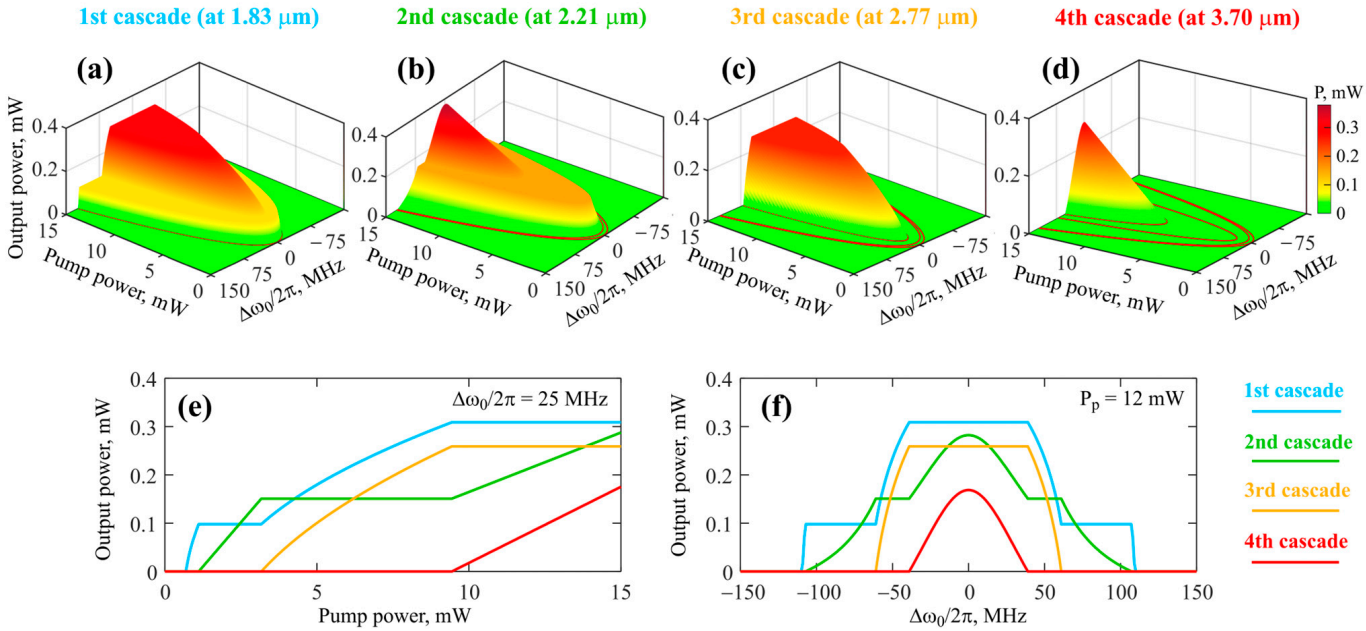

Figure 6. Output power in Raman wave as a function of pump power and detuning for the first cascade (**a**), the second cascade (**b**), the third cascade (**c**), and the fourth cascade (**d**) in a 60 μm microsphere with $Q = 1.2 \times 10^7$. Output power in Raman wave as a function of pump power for all cascades at fixed detuning (**e**). Output power in Raman wave vs. detuning for all cascades for a fixed pump power of 12 mW (**f**).

For a better understanding of the obtained results, we fixed the detuning value ($\Delta\omega_0/(2\pi) = 25$ MHz) and considered how the powers of the Raman waves depended on the pump power. The results are shown in Figure 6e. We also analyzed how the powers in Raman waves depended on the detuning at a fixed pump power of 12 mW (Figure 6f). It is seen that when the pump power is sufficient for the generation of a wave only in the first cascade, the power of this Raman wave increases nonlinearly. When two Raman waves can be generated in the system (in the first and second cascades), the wave power in the first cascade at 1.83 μm remains constant, while the wave power in the second cascade at 2.21 μm increases linearly with increasing pump power. When Raman waves are generated in the system in three cascades, the wave power in the second cascade remains constant, while the powers in the first and third (at 2.77 μm) cascades increase with increasing pump power. When the pump power is sufficient to generate waves in all four cascades, the wave powers in the first and third cascades do not change, while the powers in the second and fourth (at 3.7 μm) cascades increase linearly with increasing pump power. It should be noted that this behavior of the powers in Raman waves in different cascades is consistent with the results of the reference [16].

4. Discussion and Conclusions

To conclude, we proposed and theoretically investigated multicascade Raman microlasers based on soft tellurite TeO_2–WO_3–Bi_2O_3 glass WGM microresonators which can operate in the near-IR and mid-IR with a narrow-line pump in the telecommunication range. We assumed that a tellurite fiber taper (transparent in the near-IR and mid-IR) can be used to couple the pump light into a microsphere and extract the generated Raman waves from it. We considered a realistic design and performed a detailed theoretical study using the experimental parameters of the glass reported in [22] and the experimental parameters of the microspheres produced previously from a similar tellurite TeO_2–WO_3–La_2O_3 glass [23]. Thanks to the large Raman gain (120 times exceeding the maximum Raman gain of silica glass) and a huge Raman frequency shift of 27.5 THz for this glass (against 13.2 THz for silica glass), the Raman waves at 1.83 μm, 2.21 μm, 2.77 μm, and 3.7 μm in the first, second,

third, and fourth cascades, respectively, with a pump wavelength of 1.57 μm were demonstrated. Previously, we experimentally achieved two-cascade Raman lasing in a 30 μm microsphere made of TeO_2–WO_3–La_2O_3 glass with the frequency shift ~21 THz [23]. The Raman wavelength in the second cascade was 2.01 μm [23]. Experimental measurements were in good agreement with simulations performed using a similar general approach, confirming the validity of our model. Here, we extended the theoretical model to include Raman cascades beyond the second order. We believe that multicascade Raman lasing can be observed in optimized experiments.

We also solved a thermo-optical problem using the finite element method to show that the temperature of a soft glass microresonator heated due to partial thermalization of pump power remains below the glass transition temperature (for reasonable pump powers). The smaller the microsphere, the higher the temperature increase. It was demonstrated that the maximum temperature increase in the equatorial region, where the main pump thermalization occurs, exceeds the temperature increase averaged over the entire microsphere by only about 10%.

To describe multicascade Raman lasing, we used the coupled mode theory. We analyzed in detail the influence of different factors on the characteristics of the generated Raman waves, such as microsphere diameters, Q-factors, pump powers, and detuning of the pump frequency from exact resonance. The higher the Q-factor, the lower the pump power threshold for Raman lasing. The larger the microsphere, the higher the pump power threshold. So, on the one hand, small microspheres seem to be most suitable for multicascade Raman lasing. On the other hand, the temperature increase for them is maximal. Therefore, we can say that for the proposed experimental implementation, it may be better to work with microspheres with intermediate diameters (about 60 μm), for which the pump power thresholds are quite low and, at the same time, the temperature remains below T_g.

To the best of our knowledge, the mid-IR tellurite glass Raman WGM microlasers have not been studied before. We believe that this work can serve as a guide in the development of promising miniature multicascade mid-IR WGM microlasers, which may find many applications.

Author Contributions: Conceptualization, E.A.A.; methodology, E.A.A. and M.P.M.; software, E.A.A. and M.P.M.; validation, E.A.A., M.P.M. and A.V.A.; formal analysis, E.A.A., M.P.M. and A.V.A.; investigation, E.A.A. and M.P.M.; data curation, E.A.A. and M.P.M.; writing—original draft preparation, E.A.A.; writing—review and editing, M.P.M. and A.V.A.; visualization, E.A.A. and M.P.M.; supervision, E.A.A.; funding acquisition, E.A.A. All authors have read and agreed to the published version of the manuscript.

Funding: This research was funded by the Russian Science Foundation, grant no. 20-72-10188-P.

Institutional Review Board Statement: Not applicable.

Informed Consent Statement: Not applicable.

Data Availability Statement: Data underlying the results presented in this article may be obtained from the authors upon reasonable request.

Conflicts of Interest: The authors declare no conflict of interest.

References

1. Svelto, O.; Hanna, D.C. *Principles of Lasers*; Springer: New York, NY, USA, 2010.
2. Agrawal, G.P. *Nonlinear Fiber Optics*, 6th ed.; Elsevier: Amsterdam, The Netherlands, 2019.
3. Supradeepa, V.R.; Feng, Y.; Nicholson, J.W. Raman fiber lasers. *J. Opt.* **2017**, *19*, 023001. [CrossRef]
4. Rong, H.; Xu, S.; Cohen, O.; Raday, O.; Lee, M.; Sih, V.; Paniccia, M. A Cascaded Silicon Raman Laser. *Nat. Photon.* **2008**, *2*, 170–174. [CrossRef]
5. Spence, D.J. Spectral Effects of Stimulated Raman Scattering in Crystals. *Prog. Quantum Electron.* **2017**, *51*, 1–45. [CrossRef]
6. Sarang, S.; Richardson, M. Power Scaling of CW Crystalline OPOs and Raman Lasers. *Photonics* **2021**, *8*, 565. [CrossRef]
7. Kharenko, D.S.; Gervaziev, M.D.; Kuznetsov, A.G.; Podivilov, E.V.; Wabnitz, S.; Babin, S.A. Mode-Resolved Analysis of Pump and Stokes Beams in LD-Pumped GRIN Fiber Raman Lasers. *Opt. Lett.* **2022**, *47*, 1222–1225. [CrossRef]

8. Gladyshev, A.V.; Kosolapov, A.F.; Khudyakov, M.M.; Yatsenko, Y.P.; Kolyadin, A.N.; Krylov, A.A.; Pryamikov, A.D.; Biriukov, A.S.; Likhachev, M.E.; Bufetov, I.A.; et al. 4.4-μm Raman Laser Based on Hollow-Core Silica Fibre. *Quantum Electron.* **2017**, *47*, 491–494. [CrossRef]
9. Li, Z.; Pei, W.; Li, H.; Huang, W.; Li, X.; Wang, Z.; Chen, J. D_2-Filled Hollow-Core Fiber Gas Raman Laser at 2.15 μm. *Photonics* **2022**, *9*, 753. [CrossRef]
10. Reynolds, T.; Riesen, N.; Meldrum, A.; Fan, X.; Hall, J.M.M.; Monro, T.M.; François, A. Fluorescent and Lasing Whispering Gallery Mode Microresonators for Sensing Applications. *Laser Photonics Rev.* **2017**, *11*, 1600265. [CrossRef]
11. Sirleto, L. Micro and Nano Raman Lasers. *Micromachines* **2021**, *12*, 15. [CrossRef]
12. Brasseur, J.K.; Repasky, K.S.; Carlsten, J.L. Continuous-Wave Raman Laser in H_2. *Opt. Lett.* **1998**, *23*, 367–369. [CrossRef] [PubMed]
13. Turitsyn, S.K.; Babin, S.A.; Churkin, D.V.; Vatnik, I.D.; Nikulin, M.; Podivilov, E.V. Random Distributed Feedback Fibre Lasers. *Phys. Rep.* **2014**, *542*, 133–193. [CrossRef]
14. Vatnik, I.D.; Churkin, D.V.; Babin, S.A.; Turitsyn, S.K. Cascaded Random Distributed Feedback Raman Fiber Laser Operating at 1.2 μm. *Opt. Express* **2011**, *19*, 18486–19494. [CrossRef] [PubMed]
15. Dianov, E.M.; Bufetov, I.A.; Bubnov, M.M.; Grekov, M.V.; Vasiliev, S.A.; Medvedkov, O.I. Three-Cascaded 1407-nm Raman Laser Based on Phosphorus-Doped Silica Fiber. *Opt. Lett.* **2000**, *25*, 402–404. [CrossRef] [PubMed]
16. Min, B.; Kippenberg, T.J.; Vahala, K.J. Compact, Fiber-Compatible, Cascaded Raman Laser. *Opt. Lett.* **2003**, *28*, 1507–1509. [CrossRef] [PubMed]
17. Vanier, F.; Peter, Y.-A.; Rochette, M. Cascaded Raman Lasing in Packaged High Quality As_2S_3 Microspheres. *Opt. Express* **2014**, *22*, 28731–28739. [CrossRef]
18. Grudinin, I.S.; Maleki, L. Ultralow-Threshold Raman Lasing with CaF_2 Resonators. *Opt. Lett.* **2006**, *32*, 166–168. [CrossRef]
19. Xiong, C.; Magi, E.; Luan, F.; Tuniz, A.; Dekker, S.; Sanghera, J.S.; Shaw, L.B.; Aggarwal, I.D.; Eggleton, B.J. Characterization of Picosecond Pulse Nonlinear Propagation in Chalcogenide As_2S_3 Fiber. *Appl. Opt.* **2009**, *48*, 5467–5474. [CrossRef]
20. Slusher, R.E.; Lenz, G.; Hodelin, J.; Sanghera, J.; Shaw, L.B.; Aggarwal, I.D. Large Raman Gain and Nonlinear Phase Shifts in High-Purity As_2Se_3 Chalcogenide Fibers. *J. Opt. Soc. Am. B* **2004**, *21*, 1146–1155. [CrossRef]
21. Plotnichenko, V.G.; Sokolov, V.O.; Koltashev, V.V.; Dianov, E.M.; Grishin, I.A.; Churbanov, M.F. Raman Band Intensities of Tellurite Glasses. *Opt. Lett.* **2005**, *30*, 1156–1158. [CrossRef]
22. Okhrimchuk, A.G.; Yatsenko, Y.P.; Smayev, M.P.; Koltashev, V.V.; Dorofeev, V.V. Nonlinear Properties of the Depressed Cladding Single Mode TeO_2-WO_3-Bi_2O_3 Channel Waveguide Fabricated by Direct Laser Writing. *Opt. Mater. Express* **2018**, *8*, 3424–3437. [CrossRef]
23. Anashkina, E.A.; Andrianov, A.V. Switchable cascade Raman lasing in a tellurite glass microresonator. *ACS Photonics* **2023**, *10*, 1485–1494. [CrossRef]
24. Andrianov, A.V.; Anashkina, E.A. Tunable Raman Lasing in an As_2S_3 Chalcogenide Glass Microsphere. *Opt. Express* **2021**, *29*, 5580–5587. [CrossRef] [PubMed]
25. Smayev, M.P.; Dorofeev, V.V.; Moiseev, A.N.; Okhrimchuk, A.G. Femtosecond Laser Writing of a Depressed Cladding Single Mode Channel Waveguide in High-Purity Tellurite Glass. *J. Non-Cryst. Solids* **2018**, *480*, 100–106. [CrossRef]
26. Oraevsky, A.N. Whispering-Gallery Waves. *Quantum Electron.* **2002**, *32*, 377–400. [CrossRef]
27. Farnesi, D.; Cosi, F.; Trono, C.; Righini, G.C.; Conti, G.N.; Soria, S. Stimulated Anti-Stokes Raman Scattering Resonantly Enhanced in Silica Microspheres. *Opt. Lett.* **2014**, *39*, 5993–5996. [CrossRef]
28. Sayson, N.L.B.; Webb, K.E.; Coen, S.; Erkintalo, M.; Murdoch, S.G. Widely Tunable Optical Parametric Oscillation in a Kerr Microresonator. *Opt. Lett.* **2017**, *42*, 5190–5193. [CrossRef]
29. Marisova, M.P.; Andrianov, A.V.; Leuchs, G.; Anashkina, E.A. Dispersion Tailoring and Four-Wave Mixing in Silica Microspheres with Germanosilicate Coating. *Photonics* **2021**, *8*, 473. [CrossRef]
30. Incropera, F.P.; DeWitt, D.P.; Bergman, T.L.; Lavine, A.S. *Fundamentals of Heat and Mass Transfer*, 6th ed.; John Wiley & Sons: Hoboken, NJ, USA, 2006.
31. Jiang, X.; Yang, L. Optothermal dynamics in whispering-gallery microresonators. *Light Sci. Appl.* **2020**, *9*, 24. [CrossRef]
32. Andrianov, A.V.; Anashkina, E.A. Experimental Demonstration of Kerr Optical Frequency Comb Generation in a Tellurite Microsphere. *Opt. Lett.* **2023**, *48*, 1862–1865. [CrossRef]